


RESEARCH ARTICLE

About drying phenomena of fuel cell and electrolyzer CCM inks: Selectivity of the evaporation of 1-propanol/water mixtures

Philipp Quarz  | Nadine Zimmerer | Philip Scharfer | Wilhelm Schabel

Karlsruhe Institute of Technology (KIT), Thin Film Technology (TFT), Karlsruhe, Germany

Correspondence

Philipp Quarz, Karlsruhe Institute of Technology (KIT), Thin Film Technology (TFT), Kaiserstraße 12, 76131 Karlsruhe, Germany.

Email: philipp.quarz@kit.edu

Abstract

In the production of catalyst-coated membranes (CCMs) for proton-exchange membrane fuel cells and electrolyzers, the ink formulation and its processing are key factors in determining the resulting catalyst layer. Catalyst inks often contain a multicomponent solvent mixture. Selective drying, which can occur with solvent mixtures, changes the composition in the solidifying film and thus influences the microstructure of the layer that forms. The selectivity depends on the material-specific thermodynamics of the solvents and the process-related drying parameters. Different 1-propanol/water mixtures serve as the state of the art material system considered and commonly used for CCM inks. Typical solvent mixtures can be dried selectively or non-selectively, depending on the initial ink composition and humidity of the drying air. In mixtures that contain more 1-propanol than the azeotropic or arheotropic composition, the 1-propanol content accumulates in the remaining liquid; if there is less, it decreases. Increasing the preloading of the drying air with water leads to a relative water enrichment and shifts the tipping point to higher initial alcohol fractions. This behavior can be transferred to the real CCM production.

KEYWORDS

arheotrope, catalyst ink, electrode processing, mass transport, solvent mixture evaporation

1 | INTRODUCTION

1.1 | Catalyst layer formation from multicomponent inks

The production of fuel cells and electrolyzers and their costs still are crucial challenges to those promising devices [1, 2]. Especially the material costs of the key component of the systems, the catalyst-coated membrane (CCM), account for more than half of the system costs [3].

Therefore, it is important to deal effectively with the expensive materials and to optimize the processing. A deep understanding of the relevant processes involved in manufacturing is essential for good and effective products. This work deals in detail with the drying of the catalyst ink as an essential manufacturing step of the CCM.

Catalyst inks for CCM consist of a complex system of nanoparticles, an ionic polymer, and various solvents. Choi et al. [4] could not produce a homogeneous ink by using only one solvent. In addition, some common

This is an open access article under the terms of the [Creative Commons Attribution](https://creativecommons.org/licenses/by/4.0/) License, which permits use, distribution and reproduction in any medium, provided the original work is properly cited.

© 2024 The Authors. *Fuel Cells* published by Wiley-VCH GmbH.

ionomer dispersions are prepared in a solvent mixture, for example, Nafion as D520 and D2020 (Chemours [5]) or 3M Ionomer 800EW (3M [6]). As a result, numerous examples of different solvent mixtures are used in catalyst inks [7–11]. In particular, mixtures of 1-propanol and water can be found in the fuel cell and electrolyzer literature [8–23].

The used solvents and their composition have a major influence on the overall ink. For example, this affects the polarity and the permittivity of the system [17, 24, 25]. This in turn influences the form in which the ionomer is present in the ink and subsequently the rate of reagglomeration of catalyst particles [17, 21, 22, 26–30]. Thus, solvent composition influences the layer's microstructure, cell durability, and performance [22, 29, 31–33]. This is most obvious in occurring cracks, depending on solvent composition [8, 9, 11, 21, 30].

In industry and also in literature, the effect of the initial ink composition on crack formation in the resulting catalyst layer is experimentally studied, but the effects occurring during layer formation are not sufficiently addressed. In the CCM manufacturing process, after ink application, the ink composition changes due to subsequent drying of the ink [8, 9, 30].

Preloading the drying air, for example, with water in the form of relative humidity also influences the overall duration and selectivity of drying. This in turn influences the microstructure of the electrode that forms in an ink [34, 35].

This means that the final layer structure cannot be derived exclusively from the initial state of the ink, but the change in solvent composition during the solidification of the film is critical. A good initial composition is no guarantee to obtain the intended final layer structure.

During CCM production, catalyst inks are applied as thin films on a substrate and are dried subsequently. While the solvents evaporate, the catalyst layer is formed (Figure 1). In a first drying step, a period will arise, in which solvents 1 and 2 evaporate (\dot{m}_1 , \dot{m}_2) at the film surface (Figure 1a). While drying in this regime, the film shrinks, the film solidifies, and particles and ionomers arrange into a porous layer. At the end of film shrinkage (EoFS) [36], the network reaches almost its final porosity (Figure 1b). Afterward, the solvents evaporate inside the pores among the particles (Figure 1c). The microstructure is formed depending on the drying conditions [36–46]. When the film solidifies, cracks may form in the dry electrode (Figure 1d) [47, 48].

During drying, the ratio of solids (catalyst particles and ionomers) to solvents (often 1-propanol and water) changes. In addition, there is the possibility that the ratio of solvents to one another changes during and as a result of (selective) drying. This in turn influences the layer properties, affecting ionomer and particle interactions [8, 9].

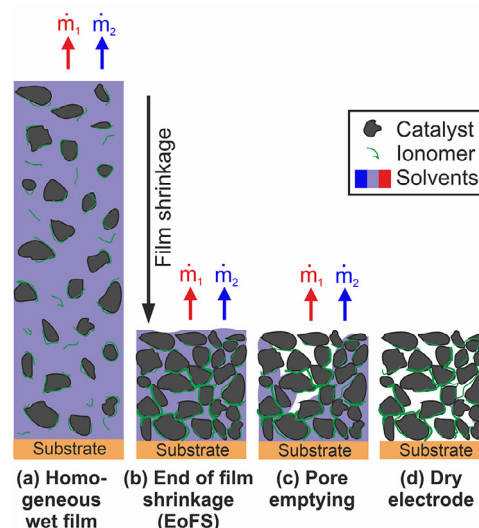


FIGURE 1 Schematic illustration of the drying steps of a catalyst ink (a–d) from a homogenous wet film to the dry electrode.

The crucial factor for the subsequent layer properties and thus the cell performance is no longer the properties of the ink in its initial composition (set during ink formulation), but of the ink with its composition during film solidification. Therefore, the evaporation of solvent mixtures needs to be better understood both phenomenologically and experimentally.

1.2 | Solvent evaporation

Starting with the vapor pressure curves of the pure solvents, 1-propanol and water show great similarities in the temperature range from 0 to 100°C [49]. Below 55°C, the curve of 1-propanol is slightly above that of water; above 55°C, it reverses.

The kinetics in the gas phase, on the other hand, differ significantly. Although the smaller water molecules have a diffusion coefficient in air of $2.50 \times 10^{-5} \text{ m}^2 \text{ s}^{-1}$ (25°C, 1.013 bar) [50], 1-propanol molecules diffuse with $1.02 \times 10^{-5} \text{ m}^2 \text{ s}^{-1}$. So 1-propanol diffuses temperature-independent 2.5 times slower than water.

For CCM production, the mixture behavior must be further considered. In hypothetical ideal 1-propanol/water mixtures, it would be expected that all initial compositions remain (nearly) constant during drying, based on the vapor pressure curves. Solvent fractions in the liquid x_1 and the gas phase y_1 are almost the same. This is shown in orange (ideal at 17.5°C) in the McCabe–Thiele diagram (Figure 2).

Because 1-propanol/water mixtures are nonideal mixtures, the interactions of the two components must be taken into account. The activity coefficients of 1-propanol and water are dependent on the composition of the binary

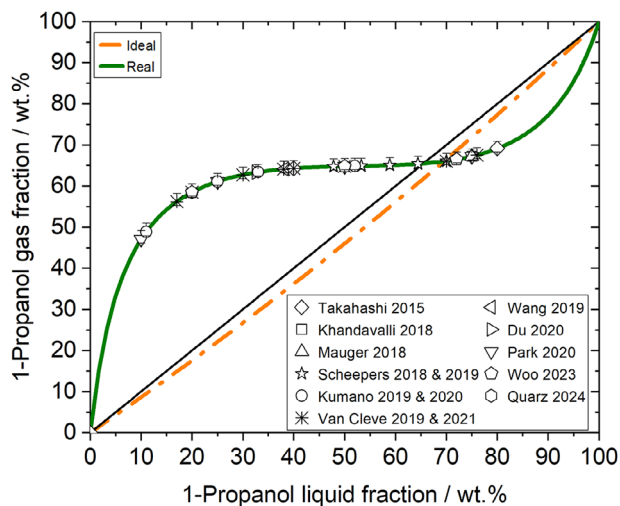


FIGURE 2 McCabe–Thiele diagram of 1-propanol/water mixtures (index 1:1-propanol) at 17.5°C. Assumed ideal (orange) and real (green) mixture behavior and common ink compositions from literature [8–21].

mixture [51]. In particular, mixing ratios with a strongly enriched component result in high values of the activity coefficients of the respective diluted component.

The thermodynamic equilibrium of the nonideal mixture shows the typical progression of an azeotropic mixture (Figure 2: green) with significant changes above and underneath the azeotropic mass composition of $x_{1,az} = 65.5$ wt.% (molar composition of $\tilde{x}_{1,az} = 36.3$ mol.%) at 17.5°C. An azeotrope means that the solvent mixture has the same composition in the vapor as in the liquid (Equation 1):

$$y_{1,az} = x_{1,az} \tag{1}$$

If evaporating at the azeotropic composition $x_{1,az}$, the composition will remain constant for the whole evaporation process. At compositions below the azeotropic point ($x_1 < x_{1,az}$), there is an enrichment of 1-propanol in the gas phase. This means that during only thermodynamically controlled evaporation, 1-propanol is preferred, and the composition of the remaining liquid changes according to a distillation process. Vice versa, on the right of the azeotropic composition, a greater amount of water is removed, and 1-propanol accumulates in the remaining liquid. For the drying of catalyst inks, it is expected that the composition of the film changes.

Some ink compositions containing 1-propanol and water solvent mixtures from the literature are plotted accordingly in Figure 2. Because y_1 over x_1 is temperature-dependent and thus also the azeotropic point itself, the literature values are plotted for a temperature range of 10–35°C. Due to evaporative cooling, this corresponds to the tem-

perature range of the resulting film temperature during convective drying with air temperatures of 20–120°C. It can be seen that very different drying behaviors are to be expected for each quoted ink due to the different positions in the diagram. Particularly in the neighborhood of the azeotropic point, temperature changes can lead to preferential 1-propanol or preferential water evaporation.

So far, literature and the previously described consider solely the thermodynamic state of the binary solvent mixture evaporation and its binary vapor. Hereby, azeotrope (from Greek *azeotropos* “boiling without change”) describes the case in the thermodynamic equilibrium where the vapor and liquid composition of the mixture are equal without an inert gas phase.

However, in drying processes, an inert gas phase, usually air, is present as a third component above the liquid. This inert gas affects the thermodynamic equilibrium and, therefore, the azeotrope. For the drying process with constant (liquid) composition, the (thermodynamic) azeotrope is replaced by the dynamic azeotrope, proposed by Riede and Schlünder [52], which is taking the dynamic gas kinetics into account.

To avoid confusion and in reference to the original Greek term, Schlünder proposed a new term called “*arheo-trope*” in a personal discussion with the co-author (W. Schabel) in 2013 after his lecture on a similar topic [53]. The idea was to substitute the boiling *zeo* with the Greek word for flow *rheo*, which refers to the relative component flow \tilde{r}_i : Schlünder’s proposed name *arheotrope* means “flow without change” and refers to $\tilde{r}_i = \tilde{x}_i$. The wording accurately describes the processes involved. Schlünder himself never published this term and passed away in 2019. In recognition of this great idea of this great scientist [54], the authors suggest introducing the term *arheotrope* and using it in further related work.

Enrichment or depletion of a component i during drying by selective evaporation can be described with \tilde{r}_i and the selectivity \tilde{S}_i according to [52, 55]. \tilde{r}_i describes the composition of the evaporation flow as the ratio between the evaporation flow of one component \dot{N}_i and the total evaporation flow \dot{N}_{total} (Equation 2). The selectivity \tilde{S}_i defines the difference between the relative component flow leaving the liquid and the current composition of the liquid phase \tilde{x}_i (Equation 3). The kinetics in the gas phase is coupled via \tilde{r}_i (Equation 4) [52, 55, 56]:

$$\tilde{r}_i = \frac{\dot{N}_i}{\dot{N}_1 + \dot{N}_2} = \frac{\dot{N}_i}{\dot{N}_{total}} \tag{2}$$

$$\tilde{S}_i = \tilde{r}_i - \tilde{x}_i \tag{3}$$

$$\dot{N}_i = \tilde{r}_i \tilde{\rho}_g A_{Ph} \beta_{i,g} \ln \left(\frac{\tilde{r}_i - \tilde{y}_i^{Ph}}{\tilde{r}_i - \tilde{y}_i^\infty} \right) \quad (4)$$

The evaporation component flux \dot{N}_i depends on \tilde{r}_i , the molar gas density $\tilde{\rho}_g$, the phase interphase A_{Ph} , and the mass transfer coefficient of the component $\beta_{i,g}$. $\beta_{i,g}$ is directly connected to the diffusion coefficient $\delta_{i,g}$. The driving gradient is the molar composition at the phase boundary \tilde{y}_i^{Ph} resulting from the thermodynamic equilibrium and the environmental composition \tilde{y}_i^∞ . \tilde{y}_i^∞ is linked to a potential preloading of component i in the drying air (e.g., relative humidity).

If $\tilde{S}_i > 0$, proportionally more of component i evaporates than was relatively present in the mixture originally and depletes in the remaining liquid. For $\tilde{S}_i < 0$, component i accumulates. If $\tilde{S}_i = 0$, and therefore

$$\tilde{r}_{i,ar} = \tilde{x}_{i,ar} \quad (5)$$

the evaporation proceeds unselectively with constant solvent composition (arheotrope, Equation 5).

Drying reduces the amount of substance N_L and mass m_L in the liquid (index: L). The actual amount of substance or mass in relation to the initial (index: 0) one results from the balances for the liquid and the gas phases (Equation 6) [52, 55].

Using the molar mass, the amount of substance and mass can be converted into each other. Without any resistance on the film side, the height ratio of the current film height h_L to the initial film height is proportional to the molar and the mass ratios (Equation 7). The change in mass measured experimentally in this work can be used to calculate a volume ratio by using the density ratio. Excess volume is neglected here, as $V_{E,max}$ is below 2% at $x_1 = 93$ wt.% [57]. Assuming a constant cross-sectional area, the height ratio of the film can be derived. The effective molar mass and density are dependent on the current composition of the film.

There is no time factor anywhere in the transformations. Increasing the (initial) film thickness prolongs the drying time without influencing the selectivity. Assuming no film-side mass transport resistance, experiments conducted in this work with film height changes on the cm scale are therefore transferable to thin films on the μm scale. More on this later in Figure 9:

$$\frac{N_L}{N_{L,0}} = \exp \int_{\tilde{x}_{1,0}}^{\tilde{x}_1} \frac{d\tilde{x}_1}{\tilde{r}_1 - \tilde{x}_1} \quad (6)$$

$$\frac{h_L}{h_{L,0}} \sim \frac{V_L}{V_{L,0}} \sim \frac{m_L}{m_{L,0}} \sim \frac{N_L}{N_{L,0}} \quad (7)$$

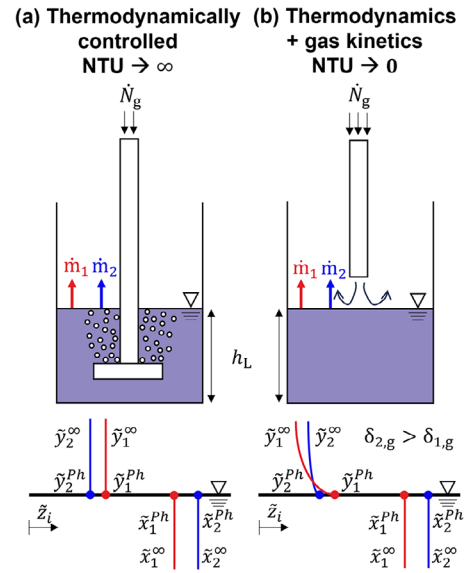


FIGURE 3 Limiting cases of drying: (a) thermodynamically controlled and (b) additionally gas-side-limited drying.

A drying process can be described with the dimensionless number of transfer units (NTU) (Equation 8), which can be understood as a dimensionless “number of time units.” It sets the evaporation flow rate in relation to the gas flow “rate” \dot{N}_g [58]:

$$NTU_{i,g} = \frac{\tilde{\rho}_g A_{Ph} \beta_{i,g}}{\dot{N}_g} \quad (8)$$

Two limiting cases can be differentiated. For $NTU_{i,g} \rightarrow \infty$, the evaporation is in thermodynamic equilibrium (thermodynamically controlled). The according drying process would be characterized by low air flows and, therefore, long residence times coupled with very high interfaces, resulting in constant concentration profiles in the gas phase. In reality, this can only be realized in a saturator, if at all (Figure 3a).

Closer to the real ink-drying step is the limiting case of $NTU_{i,g} \rightarrow 0$. The heat transport coefficient and the coupled mass transport coefficient only increase sub-proportionally with larger gas flows [49], and the boundary surfaces are much smaller. The resulting relative short residence time makes it impossible to reach the thermodynamic equilibrium. A gas-side mass transfer resistance is present, and gas kinetics become important. \tilde{y}_i^{Ph} is still defined by the thermodynamics at the phase boundary, but \tilde{y}_i changes in the gas phase through the gas kinetics (Figure 3b).

If the diffusion coefficient of one component in the drying air is significantly lower than the other, the evaporation of this component is hindered. In this example with the binary solvent mixture 1-propanol and water,

where water diffuses in air about 2.5 times faster than 1-propanol, the solvent loading ratio in the air $\tilde{y}_1^\infty/\tilde{y}_2^\infty$ compared to direct at the phase boundary $\tilde{y}_1^{\text{Ph}}/\tilde{y}_2^{\text{Ph}}$ changes. This makes it possible to influence the selectivity by the drying parameters.

Resistances on the liquid side are not taken into account here. These would cause a concentration gradient in the film over the film height and could thus influence the effective composition at the phase boundary. The assumption that no film-side mass transport resistance occurs leads to the constant compositions in the film shown in Figure 3. More information on the influence of liquid resistances can be found in Riede et al. [52].

Drying rates and the associated production times are of great interest for the processing of electrodes. Higher drying rates (HDRs) can lead to different electrode properties [39, 46, 59–62] but have an advantage over lower drying rates (LDRs) in terms of faster production times. Even the LDR when, for example, slow drying an electrode under ambient conditions in the laboratory also reflects the limiting case of $\text{NTU}_{i,g} \rightarrow 0$ and is described by gas-side controlled drying, which increases the importance of this drying case.

1.3 | Fundamentals of catalyst ink drying

Phenomenologically, the presence of several solvents results in mixture evaporation, as is also present during the drying of fuel cells and electrolysis inks. However, the processes and changes in solvent composition in catalyst inks and its effects are not yet sufficiently addressed in the fuel cell and electrolysis literature. Based on the often known azeotrope, the gas kinetics must be taken into account for an exact process description. The present work attempts to close this gap by theoretically explaining changes in ink composition during drying, which, if at all, have so far only been observed experimentally [8, 9, 30]. The explanations are supported by an experimental setup for the quantitative determination of compositions in the drying process of binary solvent mixtures, which can also be transferred to real ink drying.

2 | EXPERIMENTAL PROCEDURES

Different mixtures ($x_1 = 40.0; 60.0; 65.5; 72.0$, and 81.5 wt.%) of 1-propanol (Carl Roth GmbH; >99.5%) and purified water were mixed, and their drying behavior in two different setups was investigated. The experimental setup is described in detail in Ref. [58] and consists of a heatable liquid reservoir placed on a balance. The different drying conditions are realized first by flowing through

the liquid by a frit immersed in the liquid, realizing high residence times and large phase boundaries (thermodynamically controlled drying). Second, the drying air flows through an impinging jet nozzle above the liquid reservoir (gas-side controlled drying). The supply air is heated and can be preloaded by means of a pre-saturator.

The metered gas stream is heated to $20 \pm 1^\circ\text{C}$ for the experiments in the saturator ($\dot{V}_g = 0.1 \text{ L s}^{-1}$) and to $50 \pm 2^\circ\text{C}$ for the overflow ($\dot{V}_g = 0.4 \text{ L s}^{-1}$). The dew point of the conditioned air was at -16.6°C . This corresponds to a water preloading of $\tilde{y}_2^\infty = 0.0014$. In the studies with increased humidity, the drying air was pre-saturated with water at 11°C , resulting in $\tilde{y}_2^\infty = 0.013$.

In all experiments, the temperature of the liquid starts at 21°C and decreases during evaporation. In the overflowing setup, temperature decreases from the second to the last measurement point from 18 to 17°C , and in the additionally water-heated saturator setup, it also from 18 to 17°C . With preloading, a liquid temperature of $20.5 \pm 0.3^\circ\text{C}$ results.

The mass decrease of the solvent mixtures ($m_{L,0} = 100 \text{ g}$) and the actual mixture density ρ_{mix} (DMA 4100 M, Anton Paar) are determined. The decrease in mass is converted into a decrease in volume or height using the corresponding solvent density. The actual mixture composition can be determined from the density using the calibration (Equation 9) found in previous experiments for $10 \text{ wt.}\% < x_1 < 90 \text{ wt.}\%$ at 20°C :

$$x_1 = \frac{1008.55 \pm 1.20 - \frac{\rho_{\text{mix}}}{\text{kg m}^{-3}}}{2.01 \pm 0.02} \quad (9)$$

First measurements of the mixture evaporation of thin films in the micrometer range using inverse-micro Raman spectroscopy (IMRS) [63–65] show good agreement with the large-scale experiments carried out in the liquid reservoir here. More detailed investigations are part of further research. A transfer to the μm scale can therefore be assumed.

To transfer the binary 1-propanol/water mixture results to a real ink system, the ink components (particles and ionomer) are combined as “solids.” The ink’s initial solid content $x_{S,0}$ is fixed at $10 \text{ wt.}\%$.

3 | RESULTS AND DISCUSSION

3.1 | Thermodynamically controlled solvent mixture evaporation

Experimental conditions with low air flow, high phase boundary area, and long interaction time represent the boundary case of $\text{NTU}_{i,g} \rightarrow \infty$, resulting in thermodynamically controlled evaporation. For this case, it is

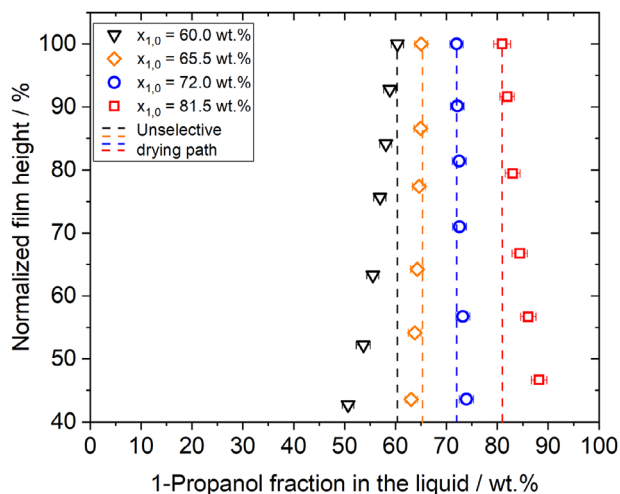


FIGURE 4 Normalized film height $h_L/h_{L,0}$ versus the mass fraction of 1-propanol x_1 of initial composition $x_{1,0} = 60.0$; 65.5; 72.0; and 81.5 wt.% at $\sim 17.5^\circ\text{C}$ ($x_{1,\text{az}} = 65.5$ wt.%) in thermodynamically controlled drying. Dashed lines symbolize unselective drying paths.

expected that a mixture below the azeotropic composition, 1-propanol evaporates preferentially. Above the azeotropic composition, an accumulation of 1-propanol in the liquid is expected (see Figure 2).

The measurements are plotted as the normalized film height $h_L/h_{L,0}$, meaning the time-dependent film height h_L relative to the initial film height $h_{L,0}$, versus the mass content of 1-propanol for mixtures with $x_{1,0} = 60.0$; 65.5; 72.0; and 81.5 wt.% (Figure 4). Consequently, all experiments start at 100% and decrease from top to bottom as the drying progresses. The dashed lines mark unselective drying and therefore a constant solvent–solvent composition, which is expected for the azeotropic composition. In the experiments, the liquids have a temperature of $17.5 \pm 0.5^\circ\text{C}$. At this temperature, the azeotropic composition is at $x_{1,\text{az}} = 65.5$ wt.% in thermodynamic equilibrium.

For $x_{1,0} = 60.0$ wt.% (below the azeotropic composition, black), as expected, a decrease in 1-propanol and an enrichment of water in the remaining liquid can be observed (e.g., $x_{1,43\%} = 50.7$ wt.%). 1-Propanol evaporates preferentially.

The measurement points for $x_{1,0} = 65.5$ wt.% (orange) show a nearly constant composition during evaporation. The gentle drift to the left toward the end of the drying process results from a slightly lower alcohol content than the azeotropic composition. No completely dry air was used in the experiments (relative air humidity $\varphi = 7.1\%$ given at 17.5°C , resp. $\tilde{y}_2^\infty = 0.0014$). With this preloading, the azeotropic composition shifts toward approx. 68 wt.% (see Figure A1). Furthermore, the liquid temperature also fluctuates between 17 and 18°C , which also slightly influences the exact location of the azeotropic point. The mentioned parameters show how difficult it is to dry non-selectively on a laboratory/production scale.

Above the azeotrope (blue and red), 1-propanol accumulates in the liquid, and water evaporates preferentially. As evaporation progresses, an increase in selective behavior can be observed. The selectivity initially increases with greater distance from the azeotropic composition (initial composition or also in the drying process), as the distance between the boiling curve and the angle bisector increases (see Figure 2).

For plotting the normalized film height, also densities of the components come into play. As 1-propanol has a density about 20% lower than water (804 compared to 998 kg m^{-3} at 20°C [49]), the density of the mixture depends on the composition at every time step. Evaporation of 1-propanol leads to a greater decrease in the remaining mixture volume or height than evaporation of the same molar quantity or mass of water. Thus, selectivity also influences volumetric film shrinkage. However, this effect is not significant for the composition changes observed here but could have an impact in the solidification step toward the end of drying.

3.2 | Solvent mixture evaporation with short interaction conditions

In a typical convective dryer, high air flows are present. In contrast to the previous case of the film with air flowing through it, the film overflow with air from above leads to a significantly smaller phase boundary here, resulting in short interaction times between air and drying film. The conditions are far distant from thermodynamic equilibrium and much closer to the limiting case $\text{NTU}_{i,g} \rightarrow 0$. Mass transport phenomena in the gas phase have to be considered.

Figure 5 shows the normalized film height of the liquid versus the mass fraction of 1-propanol for different initial mixture compositions. Drying proceeds from top to bottom, whereby the composition may change. Dashed lines symbolize unselective drying paths. The drying gas temperature of $50 \pm 2^\circ\text{C}$ results in a liquid temperature between 17 and 18°C due to evaporative cooling. The air conditions are held constant for all experiments ($\varphi = 7.1\%$ at 17.5°C , $\tilde{y}_2^\infty = 0.0014$).

For the mixture with the lowest 1-propanol content considered, $x_{1,0} = 40.0$ wt.% (green), there is an accumulation of water in the liquid ($x_{1,58\%} = 27.4$ wt.%). At $x_{1,0} = 60.0$ wt.% (black), the composition of the liquid stays constant. The three mixtures shown in orange, blue, and red with higher 1-propanol contents, $x_{1,0} = 65.5$; 72.0; and 82.0 wt.%, show an enrichment of 1-propanol in the liquid as a result of the air overflow (orange: $x_{1,61\%} = 68.3$ wt.%, blue: $x_{1,57\%} = 75.9$ wt.%, red: $x_{1,65\%} = 87.8$ wt.%). The selectivity increases with increasing evaporation, as can be seen

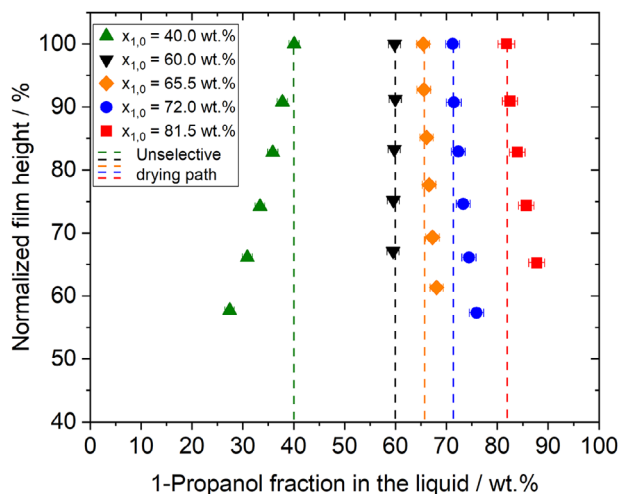


FIGURE 5 Normalized film height $h_L/h_{L,0}$ versus the mass fraction of 1-propanol x_1 of initial composition $x_{1,0} = 40.0$; 60.0 ; 65.5 ; 72.0 ; and 81.5 wt.% at $\sim 17.5^\circ\text{C}$ ($x_{1,az} = 65.5$ wt.%) in gas-side controlled drying. Dashed lines symbolize unselective drying paths.

from the ever greater shift in the measuring points during the drying process.

Compared to the first thermodynamically controlled case, the tipping point has changed to lower compositions in this experiment (Figure 6). This can be explained by accounting the gas kinetics. Water diffuses in air faster than 1-propanol, and the thermodynamically preferred 1-propanol evaporation for $x_1 < x_{1,az}$ is partly compensated.

The purely thermodynamically controlled constant composition at $x_{1,az} \approx 65.5$ wt.% shifts from the thermodynamic azeotrope to an arheotrope (ar) at lower 1-propanol fractions ($x_{1,ar} \approx 60$ wt.%). The decisive turning point

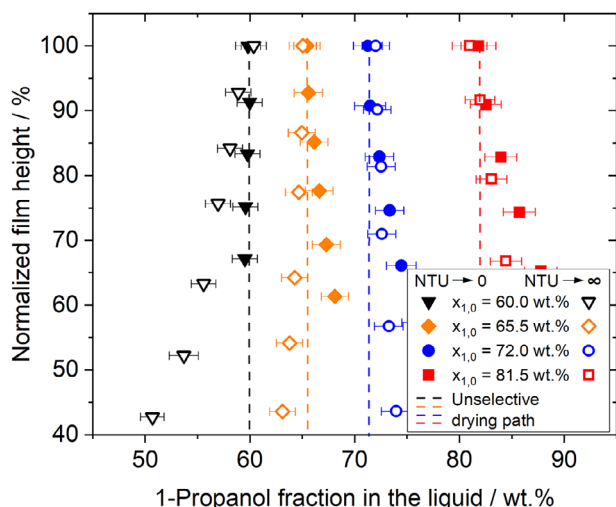


FIGURE 6 Comparison of the drying with thermodynamically (unfilled symbols) and additionally gas-side (filled symbols) controlled drying interaction times ($T_L = 17.5 \pm 0.5^\circ\text{C}$, $x_{1,az} = 65.5$ wt.%). Dashed lines symbolize unselective drying paths.

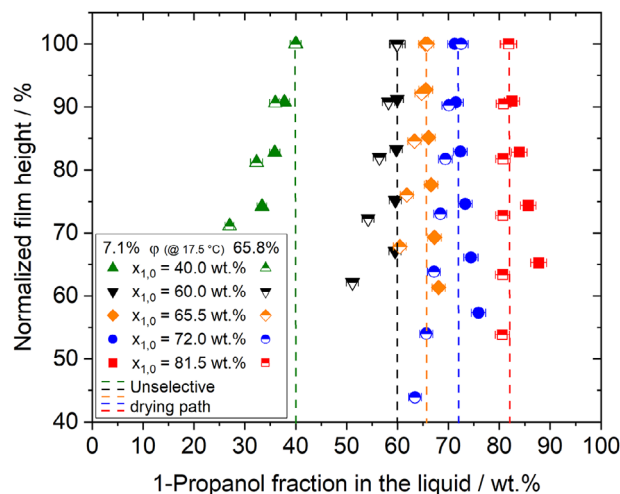


FIGURE 7 Influence of the water preloading of the drying air on the selective drying behavior in gas-side controlled drying. Filled symbols describe drying with a relative humidity of $\varphi = 7.1\%$ at 17.5°C ($\bar{y}_2^\infty = 0.0014$). Half-filled symbols derive from a preloading of $\varphi = 65.8\%$ at 17.5°C ($\bar{y}_2^\infty = 0.013$) but a thus resulting higher liquid temperature of 20.5°C .

between enrichment or depletion of one component in the mixture is no longer the azeotropic point, which is only temperature-dependent, but the arheotrope, which is also dependent on the diffusion coefficient ratio and the solvent concentration in the gas phase.

At very high gas flows with increasing but, in comparison, relatively less large mass transport coefficients, the arheotrope of 1-propanol/water can shift to a minimum of $x_{1,ar,min} = 52$ wt.% at 17.5°C and dry air. This is analytically calculated according to Thurner and Schlünder [55].

3.3 | Influence of the relative humidity of the drying air on the selectivity

The relative humidity of the drying air plays an important role in the production of CCM, for example, in the case of weather-related fluctuations in the air, for example, in winter or summer. With increasing water preloading the drying air (higher relative humidity), the water evaporation is hindered because of the lower concentration gradient (see Equation 4). In consequence, after equal time steps, less water is evaporated, and the selectivity shifts toward preferential 1-propanol evaporation (Figure 7). In addition, with the same gas temperature but with air preloading, a higher liquid temperature of $20.5 \pm 0.3^\circ\text{C}$ results (compared to $\sim 17.5^\circ\text{C}$ without).

The drying behavior of binary 1-propanol/water mixtures with and without water-preloaded drying air is compared for the same gas temperature input ($50.0 \pm 2.0^\circ\text{C}$). Again, the drying proceeds with decreasing relative film

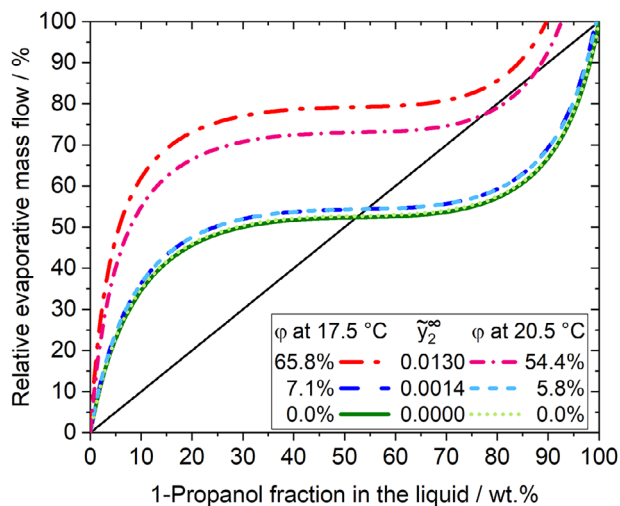


FIGURE 8 Simulated influence of water preloading of the drying air, in the case of different humidities \tilde{y}_2^∞ (0.000; 0.0014; and 0.013) at an isothermal liquid and gas phase temperature of once $T_1 = 17.5^\circ\text{C}$ and once $T_2 = 20.5^\circ\text{C}$, 1.013 bar in gas-side controlled drying, on the relative 1-propanol evaporation flux \dot{r}_1 in $\text{g s}^{-1} (\text{g s}^{-1})^{-1} \%$ versus the mass fraction of 1-propanol in the liquid x_1 . Points of intersection with the bisector describe the arheotrope.

height and possible changes in mixtures' compositions (Figure 7). The curves with preloading (half-filled symbols with $\varphi = 54.4\%$ at 20.5°C , resp. $\varphi = 65.8\%$ at 17.5°C , resp. $\tilde{y}_2^\infty = 0.013$) shift to the left compared to the measurements with lower preloading (filled symbols with $\varphi = 5.8\%$ at 20.5°C , resp. $\varphi = 7.1\%$ at 17.5°C , resp. $\tilde{y}_2^\infty = 0.0014$). The selectivity can even be reversed, if the composition is close to the arheotropic point, which can be seen in the blue and red curves. The temperature difference of 3°C alone causes a shift in the arheotropic composition of only 0.4 wt.% (see Figure 8). The significant larger changes in drying behavior can therefore be attributed to the air preloading, hindering the water to evaporate. 1-Propanol depletes in the liquid.

For understanding changes in the compositions, the influence of the preloading of air on the evaporation of 1-propanol/water mixtures is simulated according to Ref. [52], at 1.013 bar in gas-side controlled drying (limiting case of $\text{NTU}_{i,g} \rightarrow 0$) for both experimentally obtained liquid temperatures (17.5 and 20.5°C). No film-side resistance is assumed. For the preloadings of $\tilde{y}_2^\infty = 0.000$; 0.0014; and 0.013, which is equivalent to relative air humidities at 17.5°C of $\varphi = 0.0\%$ (green); 7.1% (blue); and 65.8% (red) and relative air humidities at 20.5°C of 0.0% (light green); 5.8% (light blue); and 54.4% (pink), the relative mass flow \dot{r}_1 of 1-propanol, defined here as $\dot{r}_I = \frac{m_1}{m_1 + m_2}$ in $\text{g s}^{-1} (\text{g s}^{-1})^{-1} \%$ is shown versus the liquid composition (Figure 8).

An arheotrope is given if the composition of the outgoing evaporation flux is the same as the actual liquid composition ($\dot{r}_{1,\text{ar}} = x_{1,\text{ar}}$) and lies on the bisector. For

$\dot{r}_1 < x_1$, water evaporates preferentially; for $\dot{r}_1 > x_1$, 1-propanol does, similar to the McCabe–Thiele diagram. If \dot{r}_1 becomes larger than 100%, water condenses out of the air, because $\tilde{y}_2^{\text{Ph}} < \tilde{y}_2^\infty$ and only 1-propanol evaporates. Increasing air preloading shifts the curves to higher \dot{r}_1 and the arheotropic composition to higher 1-propanol fractions.

In the case of preloading of the drying air, water remains in the liquid after the drying because the water reaches its equilibrium with the environment (simulations not ending at 100/100). As 1-propanol continues to evaporate, the angle bisector is again intersected at high x_1 values (blue and pink). This new arheotrope is called “stable,” because the driving gradients on the right and left are directed to this point [52]. Starting with an initial composition between the left arheotrope and $x_1 = 1$, drying will always end up with a final composition of the “stable” arheotrope. In this way, the selectivity can be directly influenced.

As the water preloading increases, the area of preferred water evaporation narrows between the two arheotropes. For $\tilde{y}_2^\infty > 0.011$ at 17.5°C and for $\tilde{y}_2^\infty > 0.015$ at 20.5°C , the water evaporation becomes so restricted that 1-propanol will evaporate preferred over the whole composition range. At higher preloadings, no arheotrope exists, and drying will always end up with pure water in the ink. This limiting preloading increases with higher temperatures.

At different temperatures, the position of the arheotropic point shifts. Without preloading ($\tilde{y}_2^\infty = 0.000$), here by only 0.4 wt.% (light and dark green). With increasing preloading, however, the shift becomes more pronounced. The reason for this is the decreasing concentration difference, which reacts more sensitive to a changing \tilde{y}_2^{Ph} (see Equation 4). Preloading and temperature should therefore always be considered in combination. However, the fundamental influences of preloading the drying air on the mixture evaporation behavior were shown in these experiments.

3.4 | Transfer of the results to a catalyst ink

The drying-induced changes in composition are independent of drying time t and initial film height neglecting film-side resistances (see Equations 6 and 7). The assumption of no present film-side mass transport resistances in the binary mixtures is valid. This is confirmed experimentally in Figure 9 with different starting masses, resulting in different initial film heights but otherwise the same drying conditions. The total drying time correlates with the initial film height h_0 and initial mass m_0 but has no influence on the drying path. Approximate initial heights result from composition-dependent different densities with the same starting weight of 50 resp. 100 g.

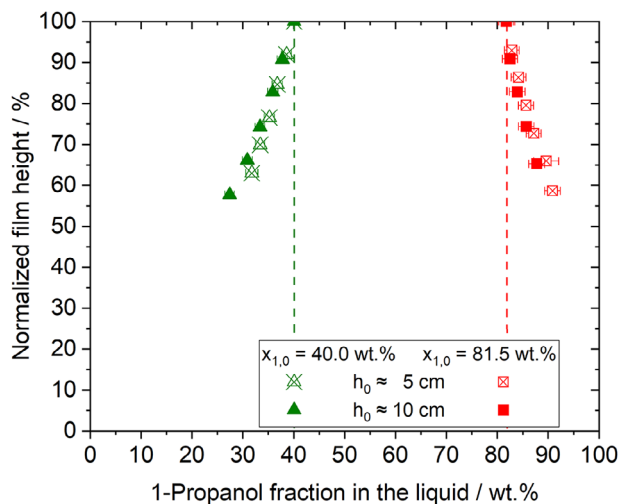


FIGURE 9 Influence of the (initial) film thickness h_0 on the selectivity.

When discussing the drying of real ink films that are only a few microns thick and composed of several solvents, it is important to consider both thermodynamics and gas kinetics. What is shown in cm-scale in this study is comparable to μm -scale in thin films, assuming no film-side resistance (Figure 10). First IMRS measurements on μm -thin films allow this conclusion to be drawn and will be conducted further in the future. For example, a film with $h_0 = 120 \mu\text{m}$ dries twice as long than a film with the same initial composition but $h_0 = 60 \mu\text{m}$. Accordingly, the composition of the film with $h_0 = 120 \mu\text{m}$ after 30 s corresponds to the composition of the film with $h_0 = 60 \mu\text{m}$ after 15 s, as the film thickness has no influence on the selectivity of drying.

Furthermore, the experiments with the (large-volume) binary solvent mixture can be applied to the drying of a

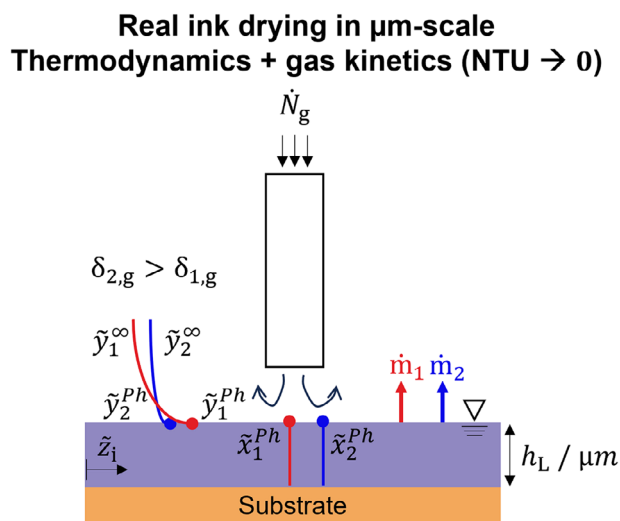


FIGURE 10 Thin film drying is affected by both thermodynamics and gas kinetics.

catalyst ink. The binary data (Figure 5) agree well qualitatively and quantitatively with the results observed during the drying of thin films of real catalyst inks containing particles and ionomers by Scheepers et al. [8, 9]. Film-side resistances seem not to occur (in the first drying stage). For this purpose, the results of this study are theoretically applied to an ink with an initial solid content (catalyst and ionomer) of $x_{S,0} = 10 \text{ wt.}\%$.

In the case of this transfer, there are some simplifications. The dissolved polymer may influence the phase equilibria [66–73]. Furthermore, the drying process changes in a porous structure at the end of ink drying. Film-side resistances have to be considered at this point [36, 37]. Moreover, geometric effects can influence selective evaporation [74].

However, most of the solvents evaporate during the first drying period, that is, until the EoFS is reached (see Figure 1). In this drying stage, the evaporation is not or just slightly influenced by these restricting parameters. Here, a solid content at EoFS of $x_{S,\text{EoFS}} \approx 60 \text{ wt.}\%$ is calculated for typical catalyst layer porosities and material densities, according to Ref. [36]. Up to this point, the drying can be approximated by the binary solvent evaporation experiments.

The drying is similar to the solvent mixture experiments. $h_L/h_{L,0}$ corresponds to film shrinkage during drying. High air flows (comparable to HDR conditions) and low air flows (comparable to LDR conditions) in the convective catalyst layer drying process refer to the gas-side controlled limiting case.

The drying paths of inks with two solvents and one solid are shown in Figure 11 as a triangular diagram. The composition of the inks in wt.% is based on the solvent compositions of the binary experiments with gas-side controlled drying (limiting case $\text{NTU}_{i,g} \rightarrow 0$) and 7.1% relative humidity at 17.5°C (see Figure 5). Drying starts from bottom with a solid content of $x_{S,0} = 10 \text{ wt.}\%$ (90 wt.% solvents) to top ($x_{S,\text{end}} = 100 \text{ wt.}\%$). Meanwhile, due to selective evaporation of the solvents, solvent–solvent ratios change. The first drying part until EoFS is highlighted yellow. From EoFS, further factors can influence the drying process, the microstructure may form, and cracks may appear. The drying process–dependent solvent–solvent ratio plays a decisive role here.

As in Figure 5, the composition of the ink with the arheotropic composition (black) follows the unselective evaporation path, seen in the straight line progression. With an initial composition with little 1-propanol (green), the alcohol evaporates preferentially and subsequently water (affecting the solvents) accumulates during drying. The total solid content increases consistently, and thus, ultimately the water content also decreases. Figure 11 on the left schematically illustrates a shrinking film with

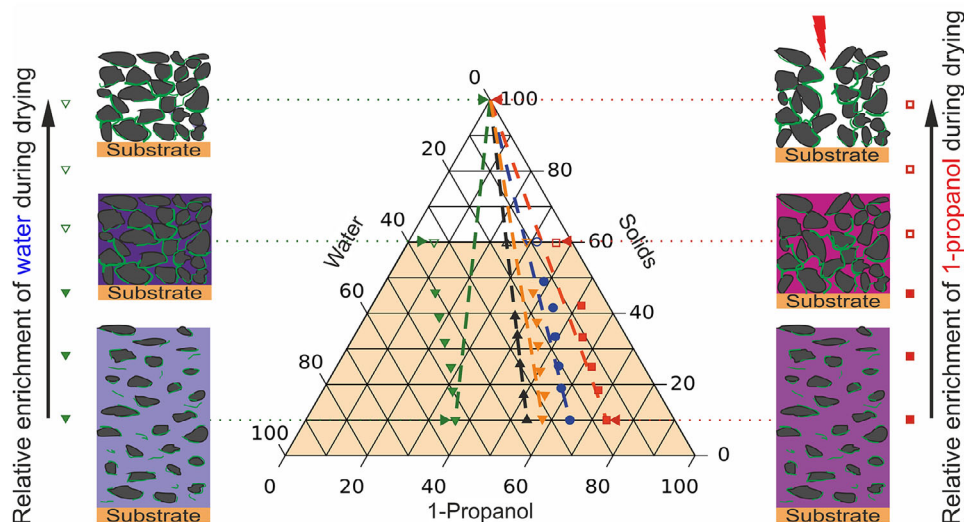


FIGURE 11 Derived drying paths of catalyst inks with an initial solid content of 10 wt.% and different starting solvent compositions in gas-side controlled drying. Dashed lines symbolize unselective drying paths. From the end of film shrinkage (EoFS, $x_{S,EoFS} \approx 60$ wt.%), cracks may appear depending on the actual composition.

the solvents that becomes less dense and more blue (water-rich).

Vice versa for inks with initial more 1-propanol than in the arheotrope (orange, blue, red). The relative 1-propanol content (affecting the solvents) increases. This is shown schematically in Figure 11 on the right-hand side with the solvent becoming less and more reddish. Thus, changing the solvent composition effects the solids (particles and ionomer). The solids arrange themselves differently, resulting in a modified microstructure, and in the red example here, a crack forms in the dry electrode.

3.5 | Possible influence on crack formation

A major challenge in the production of CCM is the formation of cracks during drying [8, 9, 11, 21, 75]. As described above, cracks may form when the porous layer solidifies, and critical stresses might occur. The main factors influencing the critical stresses are the overall evaporation rate, pore radii, surface tensions, and the liquid/solid contact angle occurring in the pores [47]. All these depend on the composition of the solvents. In addition, the present form of the ionomer acting as a stress-resistant binder [76] is also influenced by the solvents [26].

The expected area of film solidification, where cracks may occur, is marked white in the triangle diagram in Figure 11. As the solvent composition has a significant and crucial influence on the particle and ionomer modifications and properties, it stands to reason that the composition of the ink at the critical moment for crack for-

mation in particular is decisive in whether cracks occur or not. Depending on the starting composition and the drying process, different drying paths result, which lead to different ink compositions at EoFS (unfilled symbols) and afterward. These, however, are the relevant compositions that determine microstructure formation.

As a consequence, it can be concluded that, for a well-founded understanding of crack and general layer formation, the composition of the ink is relevant at the critical moment during the drying process, and this can be influenced by the process. The aspects of mixture evaporation must be carefully considered in each ink formulation.

3.6 | Aspects for the drying of CCM coating inks

For a better process understanding, a knowledge of the drying path is necessary. This includes drying temperature, air flow rates with heat and mass transfer coefficients, and preloadings of the drying air, as well as the thermodynamic solvent and solid interactions. While drying in a “simple oven” without knowing those data, it is not possible to draw the correct conclusions. Precise knowledge of the ink drying is needed to control the drying process in an event of disturbances or deviations in the formulation or the process itself.

In the case of 1-propanol/water mixtures, the initial composition has a huge effect due to large changes in the activity coefficients. The relative position to the arheotrope is crucial for process handling. Compositions in a further distance to the arheotrope have a clear drying path. Close

to the arheotrope, they are susceptible to even small system changes.

Scheepers et al. [9] showed experimentally that higher temperatures lead to faster drying but have no large effects on the drying path, except for compositions near the arheotrope. Below 55°C, the vapor pressure curves are very close for 1-propanol and water. Due to evaporative cooling, this is the relevant range even at high air temperatures. However, (slightly) increasing liquid temperature accelerates the drying. In addition, an increase in air temperature increases the diffusion coefficients and thus the evaporative fluxes, but not the ratio between them [50].

As shown in Figure 6, the flow conditions affect the drying paths in a first step. The strength of the gas kinetic influence depends on this. Starting from the thermodynamic equilibrium, which is not relevant for real ink drying, an arheotrope always prevails in a 1-propanol/water drying process. At very high overflow velocities of the drying air and short interaction times (typical conditions found in a convective dryer), there is a limit above which the drying path becomes independent of the flow conditions. Comparable to higher temperatures, however, the drying time can be further reduced.

Preloading of the drying air slows down or inhibits the evaporation of the preloaded component. It is possible to shift the position of the arheotrope almost arbitrarily. Additionally, a second arheotrope is formed. With initial composition to the right of the first arheotrope, drying ends at this second “stable” arheotrope, provided that drying proceeds undisturbed for long enough. Thus, a specific composition can be targeted at the beginning of the EoFS.

Water preloading in particular can vary considerably depending on the weather or season in the case of unconditioned drying air and thus significantly influence the drying paths of the ink and thus also the potential formation of cracks. In positive terms, it is also possible to intervene actively in the process in a target-oriented manner.

To fully consider the process understanding of CCM manufacturing, it is helpful taking a look from above, away from the sole consideration of the drying. The aspect of changing the ink composition with respect to the solvents in the application process is not exclusively due to drying. Particularly in the case of direct membrane coating, there are interactions between the membrane and the solvent mixtures in the form of membrane swelling [77]. This also leads to selectivity in the absorption of the solvents in the membrane [67, 78]. Preloading of the drying air influences both the drying itself and the membrane configuration and therefore the selectivity of solvent uptake from the ink into the membrane [79].

4 | CONCLUSION

1-Propanol/Water mixtures are commonly used in catalyst inks for fuel cell and electrolyzer CCM and represent a complex case of mixture evaporation. Although the vapor pressure curves are very close together over a wide temperature range, differences in the drying behavior occur when the intermolecular interactions are taken into account of the real mixture. In thermodynamic equilibrium, an azeotrope prevails at $x_{1,az} = 65.5$ wt.% (17.5°C).

In drying experiments, selective drying can be observed depending on the relative position of the composition to the azeotropic point. For $x_1 < x_{1,az}$, 1-propanol evaporates preferred and depletes in the remaining liquid. For $x_1 > x_{1,az}$, selectivity is in favor of water, and 1-propanol enriches in the liquid. Selective evaporation becomes more pronounced as the drying process continues. With the small water preloading of the drying air in the experiments, the azeotrope shifts to a value closer to 72 wt.%.

Due to a change in the drying conditions caused by a high drying air flow compared to less higher mass transfer coefficient and a smaller surface area, the kinetics of the evaporating components in the gas phase must be taken into account. The thermodynamic azeotrope becomes an arheotrope close to 60 wt.% in these experiments. As the water kinetics are larger than the 1-propanol kinetics, the arheotrope shifts to the left. With the flow conditions, the tipping point can be shifted in a certain range to a theoretical minimum of 52 wt.% (dry air).

In addition, the preloading of the drying air significantly affects the selectivity. Water preloading reduces water evaporation and leads to a shift of the arheotrope to higher 1-propanol fractions.

The selectivity depends on the relative position of the formulation to the arheotropic point. Any change in the position of it influences the relative reference and thus affects the drying path.

Solvent mixture experiments can be transferred to real ink drying. Most of the solvents evaporate in the first drying step, where the transfer is qualitatively justified. Formulation- and process-dependent selective evaporation continuously changes the film composition. With the influence of solvent composition and drying dynamics on potential cracking in the forming electrode, it is therefore relevant to consider or even actively influence these changes. As an outlook, the ionomer influence on the phase equilibrium and film-side transport resistances also in the order of magnitude of thin films will be investigated in further studies.

Nomenclature

Latin letters

A	surface area/m ²
h	film height of the liquid/ μm
m	mass/g
\dot{m}	mass flow/g s ⁻¹
N	amount of substance/mol
\dot{N}	molar flux/mol g ⁻¹
NTU	number of transfer units/-
\dot{r}	relative evaporative mass flow/g s ⁻¹ (g s ⁻¹) ⁻¹ %
\tilde{r}	relative evaporative molar flow/mol s ⁻¹ (mol s ⁻¹) ⁻¹ %
S	gravimetric selectivity/-
\tilde{S}	molar selectivity/-
T	temperature/°C
t	time/s
V	volume/mL
\dot{V}	gas flow/L s ⁻¹
x	mass fraction in the liquid/wt.%
\tilde{x}	molar fraction in the liquid/mol.%
y	mass fraction in the gas phase/wt.%
\tilde{y}	molar fraction in the gas phase/mol.%
\tilde{z}	molar fraction/mol.%

Greek letters

$\beta_{i,j}$	mass transfer coefficient of component i in medium j /m s ⁻¹
$\delta_{i,j}$	diffusion coefficient of component i in medium j /m ² s ⁻¹
ρ	density/kg m ⁻³
$\tilde{\rho}$	molar density/mol m ⁻³
φ	relative humidity of the drying air/%

Sub scripts

0	start
1	1-propanol
2	water
∞	bulk
ar	arheotrope
az	azeotrope
E	excess
end	end
EoFS	end of film shrinkage
g	gas
i, j	component i resp. j
L	liquid

Ph	phase boundary
max	maximum
min	minimum
mix	mixture
S	solid
total	total

ACKNOWLEDGMENTS

The authors would like to thank Lukas Löttert and Anna-Maria Steck for doing parts of the measurements and Ellen Terhorst for assisting this work.

ORCID

Philipp Quarz  <https://orcid.org/0009-0002-5070-325X>

REFERENCES

- International Renewable Energy Agency (IRENA), *Green Hydrogen Cost Reduction: Scaling up Electrolysers to Meet the 1.5°C Climate Goal*, IRENA, Abu Dhabi, UAE **2020**.
- A. Kampker, H. Heimes, M. Kehler, S. Hagedorn, P. Reims, O. Kaul, *Energy Rep.* **2023**, 9, 248–255.
- B. G. Pollet, S. S. Kocha, I. Staffell, *Curr. Opin. Electrochem.* **2019**, 16, 90–95.
- M. Choi, J. K. Kim, J. Kim, S. Yang, J.-E. Park, O.-H. Kim, Y.-H. Cho, *RSC Adv.* **2018**, 8, 36313–36322.
- Ion Exchange Materials, https://www.fuelcellearth.com/wp-content/uploads/converted_files/pdf/D520-D521-D1021-D2020-D2021-Product-Bulletin-Chemours.pdf (Accessed: December 2023).
- 3M™ Ionomers, https://www.fuelcellearth.com/wp-content/uploads/converted_files/pdf/D520-D521-D1021-D2020-D2021-Product-Bulletin-Chemours.pdf (Accessed: December 2023).
- M. B. Dixit, B. A. Harkey, F. Shen, K. B. Hatzell, *J. Electrochem. Soc.* **2018**, 165, F264–F271.
- F. Scheepers, A. Stähler, M. Stähler, M. Carmo, W. Lehnert, D. Stolten, *Coatings* **2018**, 8, 450.
- F. Scheepers, A. Stähler, M. Stähler, M. Carmo, W. Lehnert, D. Stolten, *J. Coat. Technol. Res.* **2019**, 16, 1213–1221.
- N. Kumano, K. Kudo, A. Suda, Y. Akimoto, M. Ishii, H. Nakamura, *J. Power Sources* **2019**, 419, 219–228.
- J. Park, Z. Kang, G. Bender, M. Ulsh, S. A. Mauger, *J. Power Sources* **2020**, 479, 228819.
- P. Quarz, N. Zimmerer, A.-M. Steck, P. Scharfer, W. Schabel, *Int. J. Hydrogen Energy* **2024**, 57, 789–797.
- S. Du, S. Guan, S. Mehrazi, F. Zhou, M. Pan, R. Zhang, P.-Y. A. Chuang, P.-C. Sui, *J. Electrochem. Soc.* **2021**, 168, 114506.
- M. Wang, J. H. Park, S. Kabir, K. C. Neyerlin, N. N. Kariuki, H. Lv, V. R. Stamenkovic, D. J. Myers, M. Ulsh, S. A. Mauger, *ACS Appl. Energy Mater.* **2019**, 2, 6417–6427.
- T. van Cleve, G. Wang, M. Mooney, C. F. Cetinbas, N. Kariuki, J. Park, A. Farghaly, D. Myers, K. C. Neyerlin, *J. Power Sources* **2021**, 482, 228889.
- T. van Cleve, S. Khandavalli, A. Chowdhury, S. Medina, S. Pylypenko, M. Wang, K. L. More, N. Kariuki, D. J. Myers, A. Z. Weber, S. A. Mauger, M. Ulsh, K. C. Neyerlin, *ACS Appl. Mater. Interfaces* **2019**, 11, 46953–46964.

17. N. Kumano, K. Kudo, Y. Akimoto, M. Ishii, H. Nakamura, *Carbon* **2020**, *169*, 429–439.
18. S. A. Mauger, K. C. Neyerlin, A. C. Yang-Neyerlin, K. L. More, M. Ulsh, *J. Electrochem. Soc.* **2018**, *165*, F1012–F1018.
19. S. Khandavalli, J. H. Park, N. N. Kariuki, D. J. Myers, J. J. Stickel, K. Hurst, K. C. Neyerlin, M. Ulsh, S. A. Mauger, *ACS Appl. Mater. Interfaces* **2018**, *10*, 43610–43622.
20. S. Takahashi, T. Mashio, N. Horibe, K. Akizuki, A. Ohma, *ChemElectroChem* **2015**, *2*, 1560–1567.
21. S. H. Woo, S. Kim, S. Woo, S.-H. Park, Y. S. Kang, N. Jung, S.-D. Yim, *Korean J. Chem. Eng.* **2023**, *40*, 2455–2462.
22. Q. Gong, C. Li, Y. Liu, J. Ilavsky, F. Guo, X. Cheng, J. Xie, *ACS Appl. Mater. Interfaces* **2021**, *13*, 37004–37013.
23. C. M. Baez-Cotto, J. P. Pfeilsticker, A. O. Godoy, M. Batool, S. Zaccarine, M. Wang, O. Bird, S. Pylypenko, J. Jankovic, M. Ulsh, S. Mauger, *J. Power Sources* **2023**, *583*, 233567.
24. G. Akerlof, *J. Am. Chem. Soc.* **1932**, *54*, 4125–4139.
25. M. Uchida, Y. Aoyama, N. Eda, A. Ohta, *J. Electrochem. Soc.* **1995**, *142*, 463–468.
26. T. Mabuchi, S.-F. Huang, T. Tokumasu, *Macromolecules* **2020**, *53*, 3273–3283.
27. G. Doo, J. H. Lee, S. Yuk, S. Choi, D.-H. Lee, D. W. Lee, H. G. Kim, S. H. Kwon, S. G. Lee, H.-T. Kim, *ACS Appl. Mater. Interfaces* **2018**, *10*, 17835–17841.
28. T. T. Ngo, T. L. Yu, H.-L. Lin, *J. Power Sources* **2013**, *225*, 293–303.
29. T. T. Ngo, T. L. Yu, H.-L. Lin, *J. Power Sources* **2013**, *238*, 1–10.
30. N. Hasegawa, A. Kamiya, T. Matsunaga, N. Kitano, M. Harada, *Colloids Surf., A* **2021**, *628*, 127153.
31. C.-H. Song, J.-S. Park, *Energies* **2019**, *12*, 549.
32. C. Lei, F. Yang, N. Macauley, M. Spinetta, G. Purdy, J. Jankovic, D. A. Cullen, K. L. More, Y. S. Kim, H. Xu, *J. Electrochem. Soc.* **2021**, *168*, 44517.
33. S. A. Mauger, M. Wang, C. F. Cetinbas, M. J. Dzara, J. H. Park, D. J. Myers, R. K. Ahluwalia, S. Pylypenko, L. Hu, S. E. A. Litster, *J. Power Sources* **2021**, *506*, 230039.
34. T. Suzuki, H. Tanaka, M. Hayase, S. Tsushima, S. Hirai, *Int. J. Hydrogen Energy* **2016**, *41*, 20326–20335.
35. J. Zhao, X. Li, Z.-S. Liu, *Int. J. Energy Res.* **2019**, *43*, 6799–6811.
36. S. Jaiser, J. Kumberg, J. Klaver, J. L. Urai, W. Schabel, J. Schmatz, P. Scharfer, *J. Power Sources* **2017**, *345*, 97–107.
37. J. Kumberg, M. Müller, R. Diehm, S. Spiegel, C. Wachsmann, W. Bauer, P. Scharfer, W. Schabel, *Energy Technol.* **2019**, *7*, 1900722.
38. J. Klemens, L. Schneider, E. C. Herbst, N. Bohn, M. Müller, W. Bauer, P. Scharfer, W. Schabel, *Energy Technol.* **2022**, *10*, 2100985.
39. A. Altvater, T. Heckmann, J. C. Eser, S. Spiegel, P. Scharfer, W. Schabel, *Energy Technol.* **2022**, *11*, 2200785.
40. L. Merklein, D. Daume, F. Braig, S. Schliske, T. Rödlmeier, M. Mink, D. Kourkoulos, B. Ulber, M. Di Biase, K. Meerholz, G. Hernandez-Sosa, U. Lemmer, H. M. Sauer, E. Dörsam, P. Scharfer, W. Schabel, *Colloids Interfaces* **2019**, *3*, 32.
41. S. Raupp, D. Daume, S. Tekoglu, L. Merklein, U. Lemmer, G. Hernandez-Sosa, H. M. Sauer, E. Dörsam, P. Scharfer, W. Schabel, *Adv. Mater. Technol.* **2017**, *2*, 1600230.
42. S. Ternes, T. Börnhorst, J. A. Schwenzer, I. M. Hossain, T. Abzieher, W. Mehlmann, U. Lemmer, P. Scharfer, W. Schabel, B. S. Richards, U. W. Paetzold, *Adv. Energy Mater.* **2019**, *9*, 1901581.
43. S. Ternes, J. Mohacsy, N. Lüttke, H. M. Pham, M. Arslan, P. Scharfer, W. Schabel, B. S. Richards, U. W. Paetzold, *ACS Appl. Mater. Interfaces* **2022**, *14*, 11300–11312.
44. L. Schneider, J. Klemens, E. C. Herbst, M. Müller, P. Scharfer, W. Schabel, W. Bauer, H. Ehrenberg, *J. Electrochem. Soc.* **2022**, *169*, 100553.
45. J. Klemens, D. Burger, L. Schneider, S. Spiegel, M. Müller, N. Bohn, W. Bauer, H. Ehrenberg, P. Scharfer, W. Schabel, *Energy Technol.* **2023**, *11*, 2300267.
46. S. Jaiser, M. Müller, M. Baunach, W. Bauer, P. Scharfer, W. Schabel, *J. Power Sources* **2016**, *318*, 210–219.
47. G. W. Scherer, *J. Am. Ceram. Soc.* **1990**, *73*, 3–14.
48. K. B. Singh, M. S. Tirumkudulu, *Phys. Rev. Lett.* **2007**, *98*, 218302.
49. P. Stephan, S. Kabelac, M. Kind, D. Mewes, K. Schaber, T. Wetzels, *VDI-Wärmeatlas*, Springer Berlin Heidelberg, Berlin, Heidelberg, Germany **2019**.
50. E. N. Fuller, K. Ensley, J. C. Giddings, *J. Phys. Chem.* **1969**, *73*, 3679–3685.
51. L. K. Jang, Y.-I. Chang, *Chem. Eng. Process Tech.* **2017**, *3*, 1039.
52. T. Riede, E. U. Schlünder, *Chem. Eng. Process.* **1990**, *27*, 83–93.
53. E. U. Schlünder, presented at *Short Course Coat. Drying Thin Films*, Karlsruhe, Germany, 4th June **2013**.
54. W. Schabel, *Drying Technol.* **2022**, *40*, 1027–1028.
55. F. Thurner, E. U. Schlünder, *Chem. Eng. Process.* **1986**, *20*, 33–41.
56. F. Thurner, E. U. Schlünder, *Chem. Eng. Process.* **1985**, *19*, 337–343.
57. M. A. Saleh, S. Akhtar, M. Nessa, M. S. Uddin, M. M. H. Bhuiyan, *Phys. Chem. Liq.* **1998**, *36*, 53–65.
58. E.-U. Schlünder, *Einführung in die Stoffübertragung*, 2. Aufl., Friedrich Vieweg + Sohn, Braunschweig, Germany **1996**.
59. S. Jaiser, N. Sanchez Salach, M. Baunach, P. Scharfer, W. Schabel, *Drying Technol.* **2017**, *35*, 1807–1817.
60. J. Klemens, L. Schneider, D. Burger, N. Zimmerer, M. Müller, W. Bauer, H. Ehrenberg, P. Scharfer, W. Schabel, *Energy Technol.* **2023**, *11*, 2300338.
61. S. Jaiser, A. Friske, M. Baunach, P. Scharfer, W. Schabel, *Drying Technol.* **2017**, *35*, 1266–1275.
62. J. Klemens, A.-K. Wurba, D. Burger, M. Müller, W. Bauer, S. Büchele, O. Leonet, J. A. Blázquez, I. Boyano, E. Ayerbe, H. Ehrenberg, J. Fleischer, A. Smith, P. Scharfer, W. Schabel, *Batteries Supercaps* **2023**, *6*, e202300291.
63. W. Schabel, P. Scharfer, M. Müller, I. Ludwig, M. Kind, *Chem. Ing. Tech.* **2003**, *75*, 1336–1344.
64. D. Siebel, W. Schabel, P. Scharfer, *Prog. Org. Coat.* **2017**, *110*, 187–194.
65. W. Schabel, *Chem. Ing. Tech.* **2005**, *77*, 1915–1926.
66. L. Merklein, J. C. Eser, T. Börnhorst, N. Könnecke, P. Scharfer, W. Schabel, *Polymer* **2021**, *222*, 123640.
67. P. Scharfer, W. Schabel, M. Kind, *Chem. Eng. Sci.* **2008**, *63*, 4676–4684.
68. P. J. Flory, *J. Chem. Phys.* **1942**, *10*, 51–61.
69. P. J. Flory, *Principles of Polymer Chemistry*, Cornell University Press, Ithaca, NY **1953**.
70. M. L. Huggins, *J. Chem. Phys.* **1941**, *9*, 440.
71. W. Schabel, I. Ludwig, M. Kind, *Drying Technol.* **2004**, *22*, 285–294.
72. W. Schabel, P. Scharfer, M. Kind, I. Mamaliga, *Chem. Eng. Sci.* **2007**, *62*, 2254–2266.
73. S. Kachel, P. Scharfer, W. Schabel, *Chem. Eng. Process.* **2013**, *68*, 45–54.
74. S. Post, I. Urukova, E. Tsotsas, *AIChE J.* **2005**, *51*, 3257–3274.

75. E. Hoffmann, S. Zhang, M. Thoma, C. Damm, W. Peukert, *Particuology* **2019**, *44*, 7–21.
76. S. Holdcroft, *Chem. Mater.* **2014**, *26*, 381–393.
77. J. Park, M. Ulsh, S. A. Mauger, *Int. J. Hydrogen Energy* **2021**, *46*, 30239–30245.
78. P. Scharfer, W. Schabel, M. Kind, *J. Membr. Sci.* **2007**, *303*, 37–42.
79. L. Ma, N. Zimmerer, J. Schäfer, P. Quarz, T. Heckmann, P. Scharfer, W. Schabel, J. Fleischer, presented at FC³ – 2nd Fuel Cell Conf. Chemnitz 2022 – Saubere Antriebe. Effizient Produziert, Chemnitz, Germany, 1st June **2022**, <https://nbn-resolving.org/urn:nbn:de:bsz:chl-qucosa2-764450>.

How to cite this article: P. Quarz, N. Zimmerer, P. Scharfer, W. Schabel, *Fuel Cells* **2024**, 1–14. <https://doi.org/10.1002/fuce.202300252>

APPENDIX

INFLUENCE OF RELATIVE AIR HUMIDITY IN THE CASE OF LONG INTERACTION TIMES ON ARHEOTROPIC COMPOSITION

In the case of very long interaction times and high-phase boundary areas, gas kinetics can be neglected [52]. At a constant liquid and gas phase temperature of 17.5°C, the influence of the preloading is shown (Figure A1). The composition of the arheotrope has to contain more 1-propanol with higher water preloading of the drying air to compensate restricted water evaporation. In comparison to short interaction times (see Figure 8) at same temperature, pressure, and preloading, here arheotropic compositions are shifted more to the right. Moreover, the preloading resulting in exclusive 1-propanol evaporation is lower: here

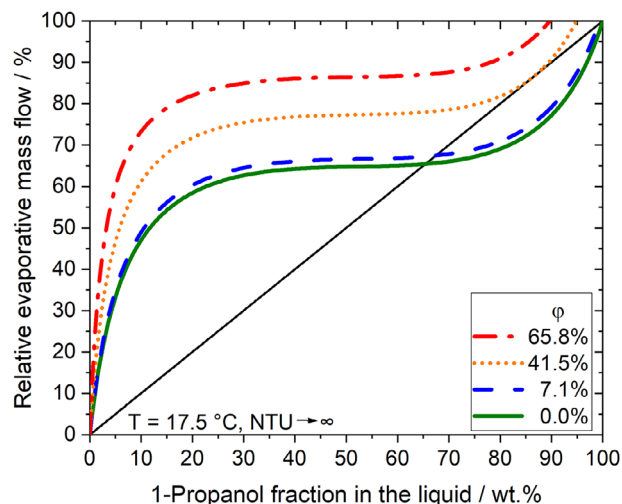


FIGURE A1 Simulated influence of water preloading of the drying air, in the case of different humidities at a constant liquid and gas phase temperature of $T = 17.5^\circ\text{C}$, 1.013 bar in thermodynamically controlled drying on the relative 1-propanol evaporation flux \dot{r}_1 in $\text{g s}^{-1} (\text{g s}^{-1})^{-1} \%$ versus the mass fraction of 1-propanol in the liquid x_1 . Points of intersection with the bisector describe the arheotrope.

$\tilde{y}_2^\infty = 0.008$ compared to 0.011 for short interaction times. This corresponds to relative air humidities of $\varphi = 41.5\%$ and 57.1% at 17.5°C . The faster water diffusion does not contribute here.

In comparison to the experimental data shown in Figure 4, the simulated arheotropic composition dried with the same preloading ($\tilde{y}_2^\infty \approx 0.0014$, respective $\varphi = 7.1\%$ at 17.5°C) fits. The assumption for the simulation was the absence of film-side resistances, which is justified by the experimental results.